Numerical Understanding on Penetration and Corrosion Behavior of CaO–Al$_2$O$_3$–MeO Slag to Al$_2$O$_3$–MgO Refractory

CHANG LIU, GUANGMEI YANG, CHONG TAN, GUANGQIANG LI, WEN YAN, ZHANMIN WANG, and QIANG WANG

To enhance the comprehension of the corrosion mechanism of refractories induced by molten slag, a 2D numerical model was developed in the present work. This model simulates the penetration of CaO–Al$_2$O$_3$–MeO slag into Al$_2$O$_3$–MgO refractory, considering capillary forces, as well as viscous and inertial resistances within the porous matrix acting on the molten slag. Experimental observations and measurements were conducted to validate the accuracy of the model. Through simulation, we visually represented the slag penetration process, highlighting the metamorphic reaction resulting from the diffusion of slag components. Notably, small aggregate particles had minimal impact on slag penetration. Instead, they were entirely enveloped by molten slag, subsequently peeling off from the refractory. The depth of penetration ($\alpha_{slag} = 0.05$, α_{slag} represents the volume fraction of liquid slag) exceeded three times the corrosion depth ($\alpha_{slag} = 0.99$). Within the region penetrated by molten slag, a portion of the refractory matrix underwent metamorphosis into the liquidus phase. Significantly, reducing porosity emerged as an effective strategy to control molten slag penetration. A 44.7 pct reduction in corrosion depth was achieved by decreasing porosity from 0.28 to 0.14. This numerical model offers valuable insights into the factors influencing refractory corrosion and presents a quantitative approach for optimizing refractory designs to enhance resistance against slag penetration.

CHANG LIU is with the The State Key Laboratory of Refractories and Metallurgy, Wuhan University of Science and Technology, Wuhan, 430081 Hubei, P.R. China and with the Key Laboratory for Ferrous Metallurgy and Resources Utilization of Ministry of Education, Wuhan University of Science and Technology, Wuhan, 430081 Hubei, P.R. China and also with the Ruipu Technology Group Co., Ltd, Lishui, 323900 Zhejiang, P.R. China. GUANGMEI YANG is with the Hunan Nonferrous Environmental Protection Research Institute Co., Ltd, Changsha 410125, P.R. China. CHONG TAN is with the The State Key Laboratory of Refractories and Metallurgy, Wuhan University of Technology, Wuhan, 430081 Hubei, P.R. China and also with the Key Laboratory for Ferrous Metallurgy and Resources Utilization of Ministry of Education, Wuhan University of Science and Technology. GUANGQIANG LI, WEN YAN, and QIANG WANG are with the The State Key Laboratory of Refractories and Metallurgy, Wuhan University of Science and Technology and also with the Key Laboratory for Ferrous Metallurgy and Resources Utilization of Ministry of Education, Wuhan University of Science and Technology. Contact e-mail: wangqiangwust@wust.edu.cn ZHANMIN WANG is with the Sinosteel Luoyang Institute of Refractories Research Co., Ltd., 471003 Luoyang, P.R. China.

Manuscript submitted November 20, 2023; accepted January 28, 2024.

Article published online February 29, 2024.

I. INTRODUCTION

Refractory materials play a pivotal role in high-temperature technologies, finding extensive application in thermal equipment and high-temperature vessels.[1] They serve as structural components and linings, enduring the severe conditions of high-temperature melts in metallurgical processes.[2] However, refractories used as furnace linings or functional elements inevitably undergo erosion and damage during metallurgical processes.[3]

The physical, chemical, and mechanical forces acting on refractories can result in deformation, softening, melting, corrosion, or cracking, not only affecting material service life but also impacting product quality and production efficiency.[4] Different types of lining refractories exhibit varied reactions with melts, with discontinuous wear being the primary mechanism in ladle refractory wear.[5] Molten slag predominantly penetrates refractories through openings, grain boundaries, and cracks driven by capillary forces, causing damage and peeling off of refractory particles.

Various parameters affect refractory corrosion, such as the temperature,[3] the environment atmosphere, the structure and composition of the refractory,[6] the wettability between melt and refractory,[7,8] and so on.

An innovative solution to enhance the performance of refractories is the utilization of lightweight Al_2O_3–MgO castables with micro-porous aggregates, which offer advantages of energy-saving and consumption reduction.[9,10] As the refractory material is in direct contact with metallurgical melts, the lightweight refractory could be used in the ladle, tundish, or other reactors. The porosity structure, heat insulation, slag attack resistance and the mechanical and thermomechanical properties of the refractory comprehensively determine its service life.[11,12] Some investigations have explored the addition of nanoscale powder[6,13] or the formation of dense coating[14] to improve the strength and the slag resistance of the refractories. In general, the macrostructure and the composition are critical parameters that influence the servicing life of refractories. Moreover, in the steelmaking process, the compound CaO–Al_2O_3–MeO (MeO represents metal oxides) slag is commonly encountered, such as the ladle refining. The interface between molten steel and molten slag is particularly susceptible to refractory corrosion,[15] followed by the interface of the slag layer, while the corrosion of molten steel on refractory is relatively weaker.[16] To evaluate the usage performance of the Al_2O_3–MgO refractory under the employ of a ladle lining, it is of great importance to investigate the interaction between the molten CaO–Al_2O_3–MeO slag and the Al_2O_3–MgO refractory.[17,18]

Investigations into slag corrosion on refractories typically involve experiments observed using X-ray radiography[19,20] or SEM (Scanning Electron Microscope) with EDS (Energy Dispersion Spectrum),[21] providing insights into penetration degree and composition distribution. Some studies have shown that aggregates with large flake-like crystal grains exhibit a thicker dissolution diffusion boundary layer and a lower dissolution rate, leading to favorable corrosion resistance of the castable.[22,23] For Al_2O_3–MgO refractories, inducing the formation of CA_6 at the border of the coarse aggregates can prevent further dissolution and enhance overall wear resistance by designing suitable castable compositions.[24,25] However, most experiments are post-detection, and then the reactions that occur could be inferred. Therefore, the information provided is limited, and due to the limitations of the opaque high-temperature reactor, the penetration of slag and heat and mass transfer behavior during the process cannot be observed. However, this information is important for studying refractory material damage. Furthermore, with the development of computing resources and numerical computing technology, many researchers have attempted to use numerical simulations[26–28] to study the corrosion process of refractories, including the slag penetration,[9] steel impact and wash,[29–31] and thermo-mechanical damage.[32,33] Compared to corrosion experiments, numerical simulation offers strong controllability and enables continuous observation, which not only saves costs and time, but also provides important information such as flow, heat transfer, and thermal stress distribution. Multiphase models and porous media models are commonly employed in these simulations. Some researchers[9] have

discovered that the average pore size of the castable with the best slag resistance was 0.5 μm using simulation CFD software. However, few investigations have focused on the chemical reaction and phase transformation induced after the slag penetrated into the refractory, which is an important aspect of the refractory damage.

To better understand the molten slag corrosion behavior on the refractory lining, a fluid-solid coupled numerical model was proposed to quantitatively analyze the permeation-driven flow, chemical reaction, mass transfer, and metamorphic reaction within the refractory. The fluid part contained the air and the molten slag, while the solid part included the aggregates and the matrix in the refractory. Furthermore, the influences of the chemical composition on the penetration and corrosion behaviors were considered. The user-defined scalars were employed in the numerical model to indicate the molten slag penetration and phase transformation processes inside the porous refractory. The user-defined memories were invoked to present the capillary permeability and the mass ratio of CaO to Al_2O_3. The corrosion situations of the refractories with different porous diameters at different positions were compared, and the mechanism of refractory corrosion was thoroughly discussed.

By establishing this numerical model, the study provides valuable insights into the penetration of the molten slag into the porous refractory and the associated metamorphic reaction. This research contributes to a deeper understanding of the corrosion mechanisms of refractories by the molten slag, and it compares the corrosion processes under different porosity levels and porous diameters, thereby shedding light on factors influencing refractory corrosion in diverse conditions.

II. NUMERICAL MODEL DESCRIPTION

The computational domain comprises both the aggregate and matrix within the refractory, forming a mesoscale system. Since the penetration processes predominantly exhibit uniform invasion, with consistent penetration depth across the same cross-section, a 2D model encompassing both the slag and refractory was employed for a more precise simulation. The model takes into account the intricacies of the complex and heterogeneous refractory structure.

A. *Assumptions*

The assumptions made in the current simulation are outlined below:

(a) The fluids, including molten slag and gas, are considered Newtonian, viscous, and incompressible.[34,35]
(b) For model simplification, the slag is treated as a liquid at 1600 °C, the aggregate as a solid, and the matrix as a porous medium. Additionally, the assumption is made that the pore radius is homogeneous without any size distribution.

(c) Except for calcium oxide and aluminum oxide, other compounds do not participate in the composition metamorphic reaction.

(d) The change in the grain size is ignored. Either the grain dissolution from slag penetration or the grain growth due to the metamorphic reaction was neglected. Thus, the constant refractory porosity and mean pore diameter were used in a specific simulation case.

(e) Irregular cracks in refractory materials are not taken into consideration.

(f) The entire system is considered to be in an isothermal state due to its confined and limited spatial extent at the mesoscale.

B. Multiphase Model

The VOF (Volume of Fluid) multiphase flow model was employed to monitor the volume fraction of each phase, providing a comprehensive depiction of the slag penetration interface profile. The continuity equation is:

$$\frac{\partial}{\partial t}\left(\alpha_q \rho_q\right) + \nabla \cdot \left(\alpha_q \rho_q \vec{u}_q\right) = 0 \qquad [1]$$

$$\sum_{q=1}^{n} \alpha_q = 1, \qquad [2]$$

where q is the phase number; α is the volume fraction of slag or gas; ρ is the density, kg/m^3; $\vec{u}$ is the velocity, m/s.

Given that the penetration process occurs through the micropores of the porous refractory, the laminar flow model was chosen for the present simulation.

The momentum transfer of the molten slag and the gas within the porous refractory was simulated using the following equation.

$$\frac{\partial}{\partial t}(\rho \vec{u}) + \nabla \cdot (\rho \vec{u}\vec{u}) = -\nabla p + \nabla \cdot \left[\mu\left(\nabla \vec{u} + \nabla \vec{u}^T\right)\right] + \vec{F}, \qquad [3]$$

where μ is the viscosity, kg/(m s); p is the pressure, Pa; $\vec{F}$ represent the source term for the momentum equation.

C. Fluid and Solid Domains Coupling

The interface between the fluid and solid parts was designated as a coupled wall. In this configuration, a coupled wall separates two fluid cell zones, with the wall zone connected to one of the cell zones and the shadow zone linked to the other.

D. Porous Media Model

The Ergun equation, encompassing viscosity and inertia resistance, was employed to characterize the hindering effect of the refractory on melt penetration. The corresponding source term of the momentum equation is expressed as follows[36,37]:

Table I. Materials Properties

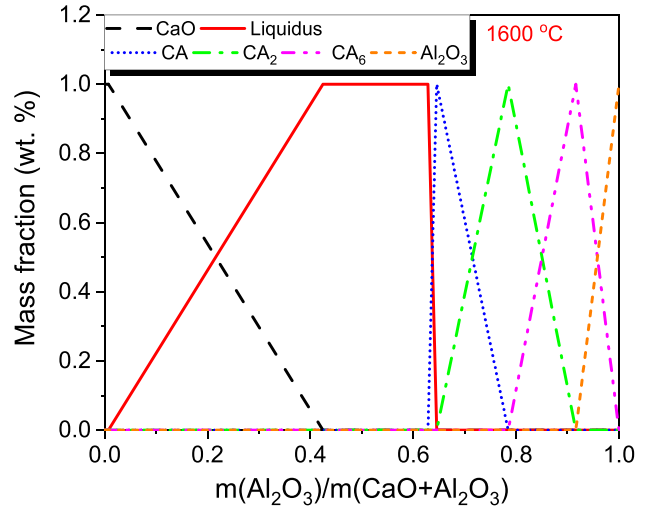| Parameters	Value
Physical Properties of Molten Slag	
Density (kg/m³)	2700
Viscosity (Pa s)	0.5 (liquid)
Surface Tension (N/m)	0.5
Contact Angle (Deg)	35[39]
Physical Properties of Refractory	
Porosity of Matrix	0.14/0.28
Pore Radius of Matrix (m)	$3.0 \times 10^{-6}/6.0 \times 10^{-6}$
Density of Aggregate (kg/m³)	3650
Physical Properties of Gas	
Density (kg·m⁻³)	1.225

Fig. 1—Phase transformation of CaO-Al₂O₃ system at 1600 °C (The data were extracted from FactSage software[40]).

$$\vec{F} = -\left(\frac{\mu}{a}\vec{u} + C_2 \cdot \frac{1}{2}\rho|\vec{u}|\vec{u}\right), \qquad [4]$$

where $1/a$ is the viscosity resistance factor and C_2 is the inertial resistance factor, calculated using the following equations.[38]

$$\frac{1}{a} = 257.36 \cdot \frac{1}{r_m^2} \cdot \left(\frac{1-\varepsilon}{\varepsilon}\right)^2 \qquad [5]$$

$$C_2 = 34909.6 \frac{1}{r_m}\frac{(1-\varepsilon)}{\varepsilon^{2.5}}, \qquad [6]$$

where r_m is the mean radius of the pore in the refractory, m; ε is the porosity of refractory.

E. Capillary Penetration Model

The pores and cracks in the refractory were simplified as a multitude of staggered capillary tubes. The driving force propelling melt penetration into the refractory was modeled as follows:

$$\vec{F} = 4\alpha_{slag}\left(1 - \alpha_{slag}\right)\frac{2\sigma\cos\theta}{r_m}, \qquad [7]$$

where α_{slag} is the volume fraction of slag; θ is the contact angle between the molten slag and the refractory, deg. The momentum source term caused by the capillary permeability is coupled to the momentum equation through a user-defined subroutine. And, the properties of the used materials are listed in Table I.

F. Phase Transformation

According to the CaO–Al$_2$O$_3$ phase diagram, the transformation of the CaO–Al$_2$O$_3$ system with the proportion of components at 1600 °C is plotted in Figure 1. The thermochemical databases were extracted from FactSage software,[40] which was verified by the Reference 21. The compound system transferred from
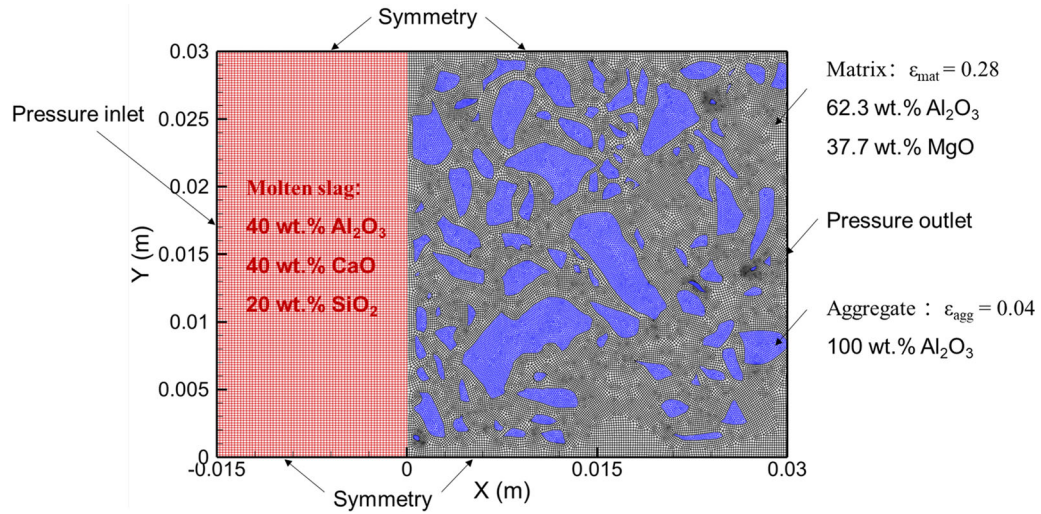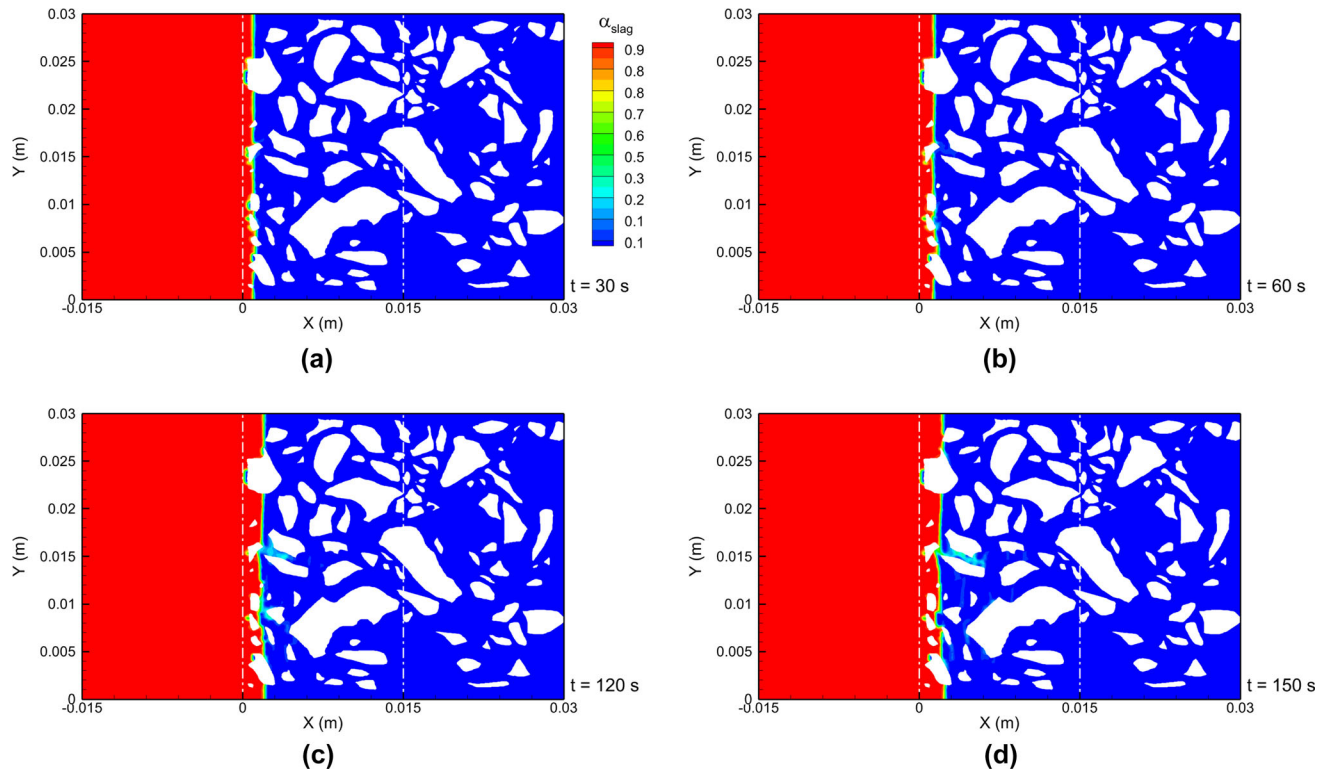

Fig. 2—2D mesh and boundary conditions.

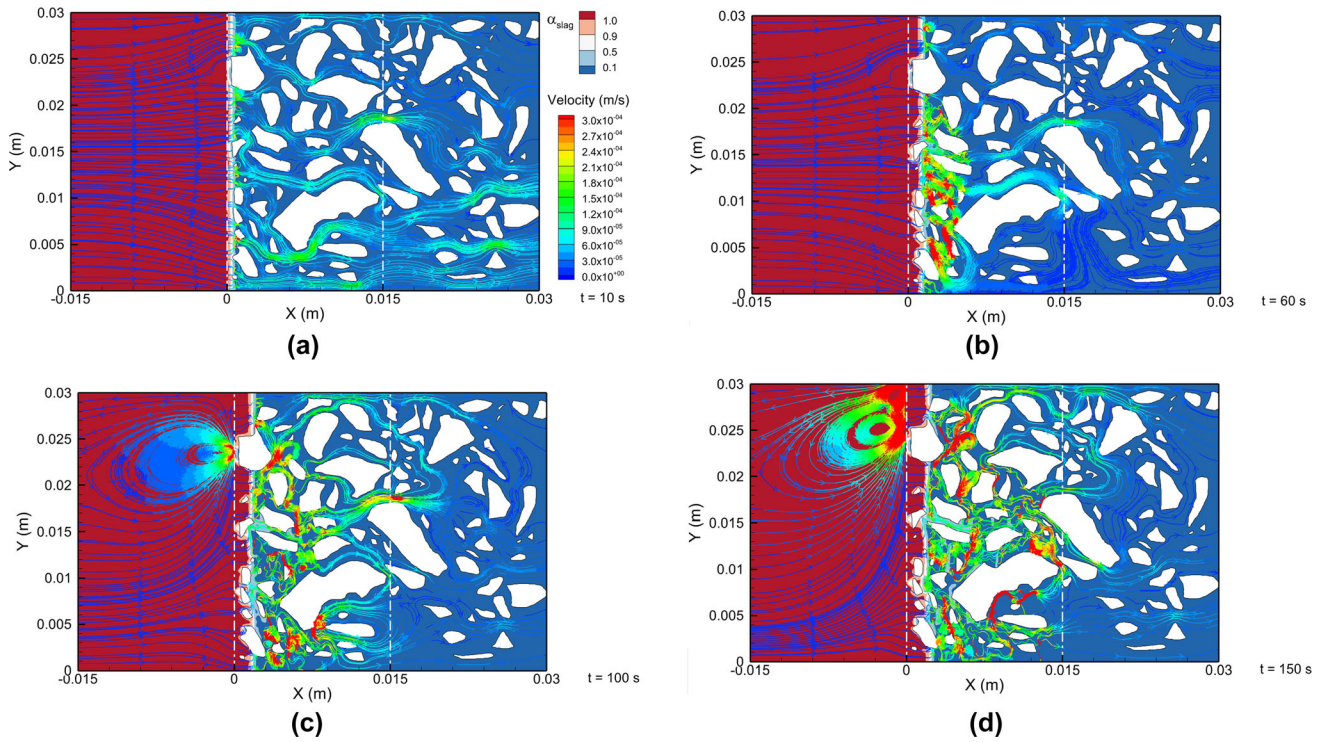Fig. 3—Penetration process of slag to the refractory: (*a*) 30 s; (*b*) 60 s; (*c*) 120 s; (*d*) 150 s.

Fig. 4—Variation of velocity streamlines in the slag and refractory with time: (*a*) 10 s; (*b*) 60 s; (*c*) 100 s; (*d*) 150 s.

$Al_2O_3 \rightarrow CaO \cdot 6Al_2O_3(CA_6) \rightarrow CaO \cdot 2Al_2O_3(CA_2) \rightarrow CaO \cdot Al_2O_3(CA)$ to liquidus with the percentage of CaO raising.

The transport equation for the employed user-defined scalar (UDS) was solved to represent the evolution of the CaO-Al$_2$O$_3$-MeO slag composition as follows.

$$\frac{\partial}{\partial t}(\rho(m_{\text{MeO}})) + \nabla \cdot (\rho \vec{u}(m_{\text{MeO}}))$$
$$= \nabla \cdot ((\rho D_{(\text{MeO})})\nabla(m_{\text{MeO}})),$$ [8]

where m_{MeO} represents the mass percent contents of CaO, Al$_2$O$_3$ or the remaining oxides that do not participate in the reaction in the molten slag; D_{MeO} is the mass diffusion coefficient of MeO component, m^2/s. The actual slag composition was computed based on their respective mass fractions, with particular attention to neglecting the influence of MeO (except for CaO or Al$_2$O$_3$) on the reaction. The resulting composition was then stored in the user-defined memory of the software used in the present simulation.

G. Solution Procedure

Based on a actual refractory section, the 2D aggregate distribution was extracted and used for geometric modeling and then meshing. And, the effect of particle size distribution may be numerically investigated in our next work. The simulation was conducted using ANSYS Fluent 2020 R1. Figure 2 illustrates the mesh and boundary conditions. Following a grid independence analysis, a mesh comprising 68,000 cells with a mean size of 0.14 mm was chosen. The molten slag was modeled as liquid, and in the refractory, the aggregate was defined
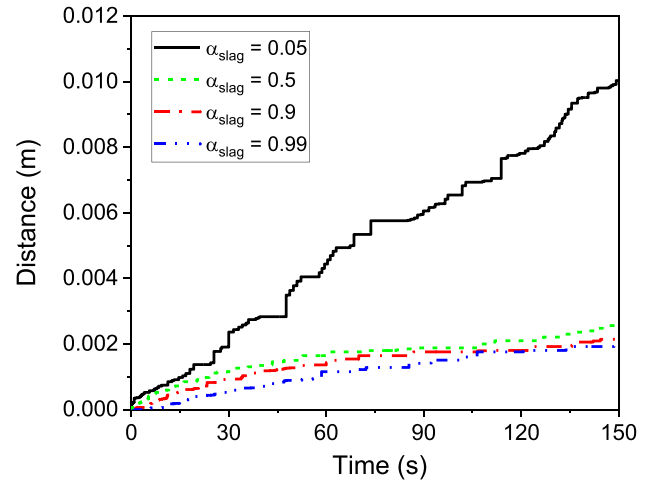

Fig. 5—Penetration of slag into refractory with different volume fraction definitions.

as solid while the matrix was treated as porous media. Additionally, the porous region consisted of both solids and gas.

The penetration of molten slag into the refractory, accounting for capillarity, interphase reaction mechanisms, and transport modes, was incorporated into the simulation using User-defined Functions (UDF). The PISO algorithm was employed for pressure-velocity coupling. Spatial discretization utilized the PRESTO! method for pressure and the first-order upwind method for momentum. Convergence criteria were set at 10^{-5}

for continuity and momentum, and 10^{-6} for the UDS equation. The calculation time step was set at 0.001 seconds.

III. PENETRATION OF SLAG INTO REFRACTORY

A. *Penetration Depth*

The penetration process of molten slag into the refractory is depicted in Figure 3, with a porosity of 0.14 and a mean pore radius of 6 μm. In the initial stage, the molten slag spreads into the refractory, and after traversing some aggregate particles, it further penetrates into the refractory interior. The presence of large aggregate particles at the refractory interface hinders the penetration of slag, as observed in the upper region of the refractory. Conversely, small aggregate particles exert a minimal effect on slag penetration, as evident in the lower region.

Notably, aggregate particles that become entirely enveloped by molten slag eventually peel off from the refractory, entering the slag. Subsequently, molten slag resumes penetration from the new interface, initiating a cyclical process. It should be pointed out that the current model falls short of achieving real-time simulation of solid material peeling. The fundamental structure of the aggregate and matrix remains fixed throughout the calculation. While the presence of completely

wrapped solid material indicates peeling, it still resides within the computational domain. Subsequently, the incoming slag continues to penetrate and react with the refractory, forming a new interface. Despite these complexities, the current model serves to imply the erosion mechanism.

The velocity streamlines in the slag and refractory are illustrated in Figure 4. At 10 s, the interface corrosion phenomenon is not pronounced, and the velocity streamlines appear relatively regular from the molten slag to the refractory. As the penetration progresses, the streamlines become more mixed and disorderly, particularly near the slag-refractory interface. The magnitude of the mixture velocity is approximately 1×10^{-4} m/s, yielding an estimated Reynolds number of 1.62×10^{-6}, affirming the suitability of the current laminar flow model for this simulation.

Four interfaces are defined based on the volume fraction of the slag phase ($\alpha_{slag} = 0.05, 0.5, 0.9,$ or 0.99). Figure 5 illustrates the variations in slag penetration distances for the farthest position of the defined interface from the initial interface. The penetration distance increases with a decrease in the selected volume fraction of molten slag. The depth of penetration exhibits a stepped pattern, determined by the grid position farthest from the interface in the X-axis. The evolution of the iso-surfaces for $\alpha_{slag} = 0.99, 0.9,$ and 0.5 is similar, with their final distances at 150 s showing little variation. Referring to Figure 3, it can be inferred that this portion
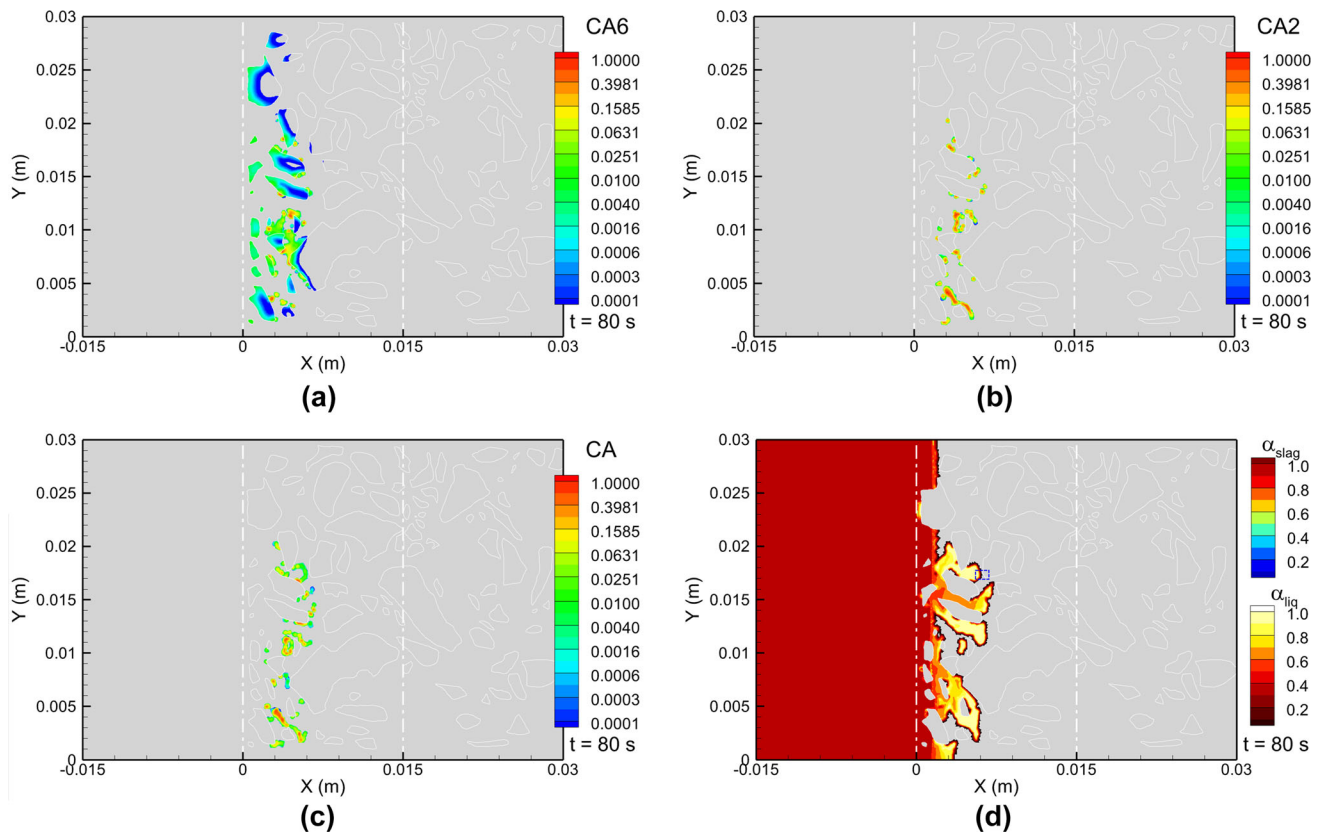

Fig. 6—Metamorphism and refractory damage: (*a*) CA$_6$; (*b*) CA$_2$; (*c*) CA; (*d*) liquidus.

has been completely damaged by molten slag, identified as the corrosion layer. However, the $\alpha_{slag} = 0.05$ iso-surface is notably higher than the others, suggesting that molten slag penetrates into the porous refractory through the pores. It is conceivable that the fundamental structure of refractory materials is preserved in this section and has not undergone severe damage. Alternatively, the chemical composition of the refractory may have changed, forming a low melting point phase that contributes to the damage. Therefore, alongside assessing the penetration degree of molten slag, consideration of metamorphic reaction becomes imperative.

B. Metamorphic Reaction

Throughout the penetration process, the slag's composition diffuses into the refractory, leading to the metamorphism in the refractory following the principle depicted in Figure 1. The metamorphism of the refractory after the molten slag ($0.6CaO–0.2Al_2O_3–0.2MeO$) penetration is displayed in Figure 6. As the aggregate is Al_2O_3, the diffusion of CaO from the slag causes a reaction with the solid Al_2O_3 aggregate, resulting in the formation of the compound CA_6 in the interior and boundary of the aggregate. Furthermore, with an increase in CaO content, small amounts of CA_2 and
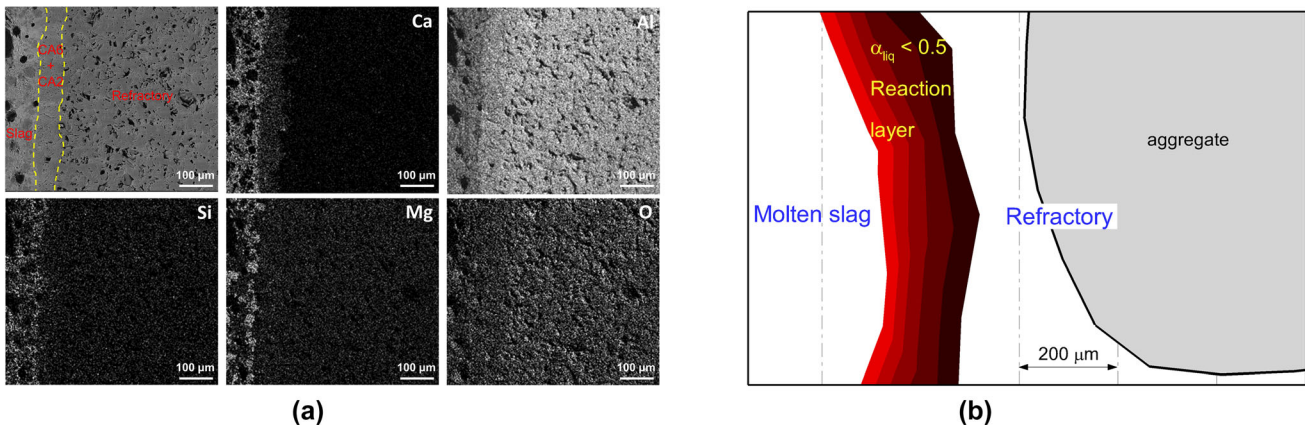

Fig. 7—Comparison of the observed and simulated reaction interfaces: (a) mapping results from experiment; (b) zoom interface from simulation.
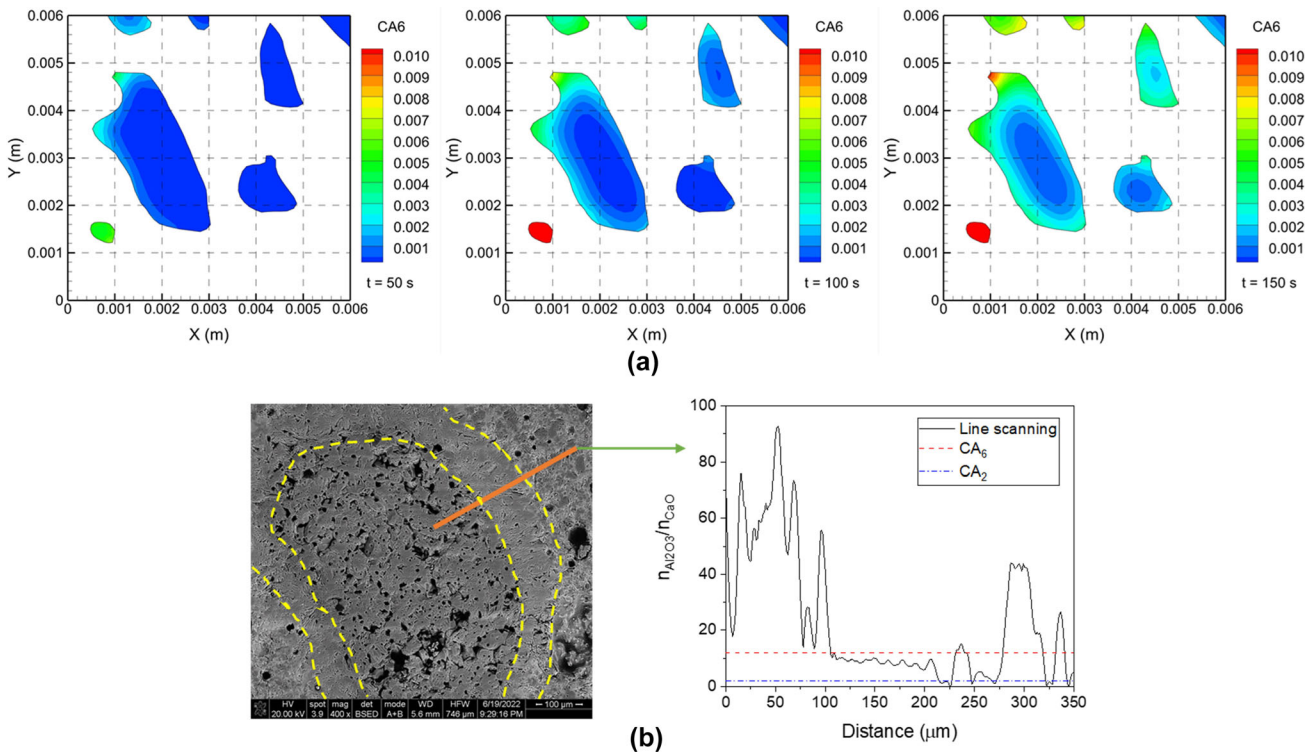

Fig. 8—Comparison of the metamorphism between the simulation and the experiment: (a) simulation; (b) experiment.

CA are generated in the matrix. Additionally, as the CaO content in the mixed phase increases during the penetration of molten slag, a liquidus phase is formed, leading to the metamorphism of the refractory.

Progressing from the molten slag to the interior of the refractory material (left to right in Figure 6), the region can be categorized into several parts: the initial part is the pure molten slag region defined by $\alpha_{slag} > 0.99$; this is succeeded by a mixing region that may contain liquid slag, CA, CA_2, or CA_6, and its composition can be calculated based on the mass ratio of CaO and Al_2O_3; the last segment is the unreacted refractory. Thus, there are two parts of liquids, one is the original slag phase defined as α_{slag}, and the other is the liquid phase transformed by reaction defined as α_{liq}. The corrosion damage layer ($\alpha_{slag} > 0.99$) and the permeable damage layer (metamorphism formed liquidus) are distinguished in Figure 6(d). Considering the necessary condition for the reaction to occur is that the slag penetrates and contact with the refractory, the liquid phase produced by the reaction should not exceed the steel slag penetration interface ($\alpha_{slag} = 0.05$) defined before. Moreover, the solid CA, CA_2, or CA_6 mainly formed near the aggregates, thus, it can be inferred that the metamorphism formed liquidus interface and the slag penetration interface ($\alpha_{slag} = 0.05$) are similar. The penetration depth is more than three times the corrosion depth, aligning with the two-volume fraction definitions ($\alpha_{slag} = 0.99$ and 0.05). Even in regions with a low volume fraction of molten slag, the refractory undergoes modification to a liquidus phase due to the diffusion and reaction of CaO and Al_2O_3. Hence, it's necessary to include the metamorphism mechanism in the refractory corrosion simulation. Since the slag penetration and the diffusion of slag components were conducted simultaneously, it is difficult to separate the permeable layer and the reactive layer. The areas with CA, CA_2, or CA_6 can be regarded as the reaction layer, primarily at the boundaries of the liquidus phase or the aggregate particles.
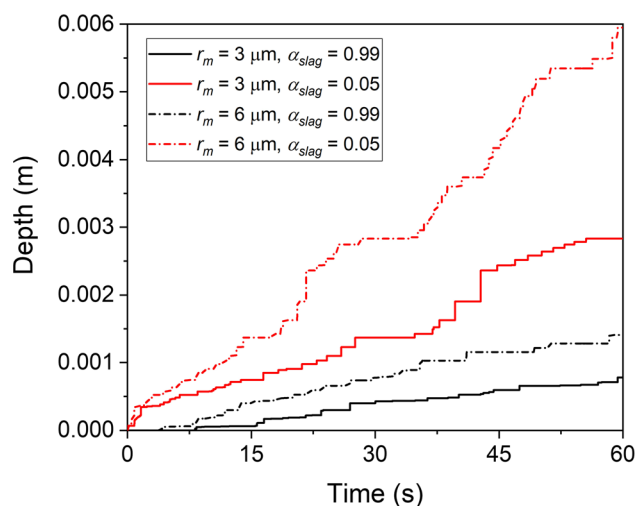
C. Model Validation

To validate the present mathematical model, a laboratory experiment was conducted involving the reaction between $CaO–Al_2O_3–MeO$ refractory and $Al_2O_3–MgO$ refractory. The refractory was immersed in melted slag and maintained at 1600 °C for 30 minutes to ensure sufficient reaction. The mapping results post-experiment are depicted in Figure 7(a), revealing a reaction interface composed of CA_6 and CA_2. The thickness of the reaction layer measured approximately 57 μm. Moreover, the zoom simulated reaction boundary layer within the blue box marked in Figure 6(d) is plotted in Figure 7(b). The areas featuring CA, CA_2, or CA_6 can be considered as the reaction layer. Consequently, regions with a liquid phase fraction between 0 and 0.5 were designated as an interaction layer between the slag and refractory. Both the calculated and observed reaction layer thicknesses are on the order of micrometers, indicating consistency between the simulation and experiment. However, the calculated reaction layer thickness is slightly larger than that observed in the experiment, possibly attributed to the current mesh not being precise enough to simulate more detailed interfaces.

Particularly noteworthy is the observation of an aggregate particle within the refractory, as shown in Figure 8. The Al_2O_3 particle is enveloped by a compound of Al_2O_3 and CaO, with the exterior predominantly consisting of slag. The reaction layer observed is similar to the results presented in Figure 7, corroborating the metamorphism mechanism $Al_2O_3 \rightarrow CA_6 \rightarrow CA_2 \rightarrow (CA) \rightarrow$ Liquidus. Importantly, the simulation replicates the same phase transformation process as observed in the experiment, providing validation for the current mathematical model.
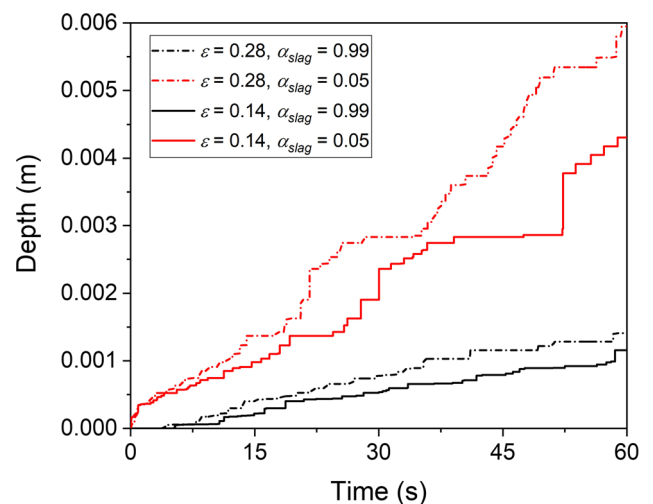

Fig. 9—Penetration of slag into refractory with different mean pore radii ($\varepsilon = 0.28$).

Fig. 10—Penetration of slag into refractory with different matrix porosities ($r_m = 6$ μm).

IV. EFFECT OF REFRACTORY PROPERTIES

Two key parameters, porosity, and mean pore size, of refractory properties were investigated in the current research. Utilizing the validated mathematical model, a comparison of the mean pore radius's effect on the corrosion process was conducted. At a porosity of 0.28, two scenarios with mean pore radii of 3 and 6 μm are depicted in Figure 9. Evidently, the penetration damage is significantly higher than the corrosion damage.

Figure 10 depicts the impact of matrix porosities on penetration depth, with a mean pore radius of 6 μm and porosities of 0.14 and 0.28. Lower porosity effectively impedes the corrosion and penetration of molten slag. During the simulation, the deepest erosion distance was determined based on the local mesh position. Consequently, this leads to variations in the position of the deepest distance at different times, contributing to a stepwise growth pattern. Notably, in Figure 10, encountering a larger aggregate causes the penetration distance to form a platform stage. Subsequently, once the slag transition passes through the larger solid particle, it rapidly spreads.

The corrosion and penetration evolution with varied refractory properties is depicted in Figure 11. It's important to note that the variable α_{slag} represents the volume fraction from the multiphase VOF model, while the variable α_{liq} represents the liquidus phase calculated from the concentration of CaO and Al$_2$O$_3$ based on the transformation mechanism (Figure 1). In this study, the
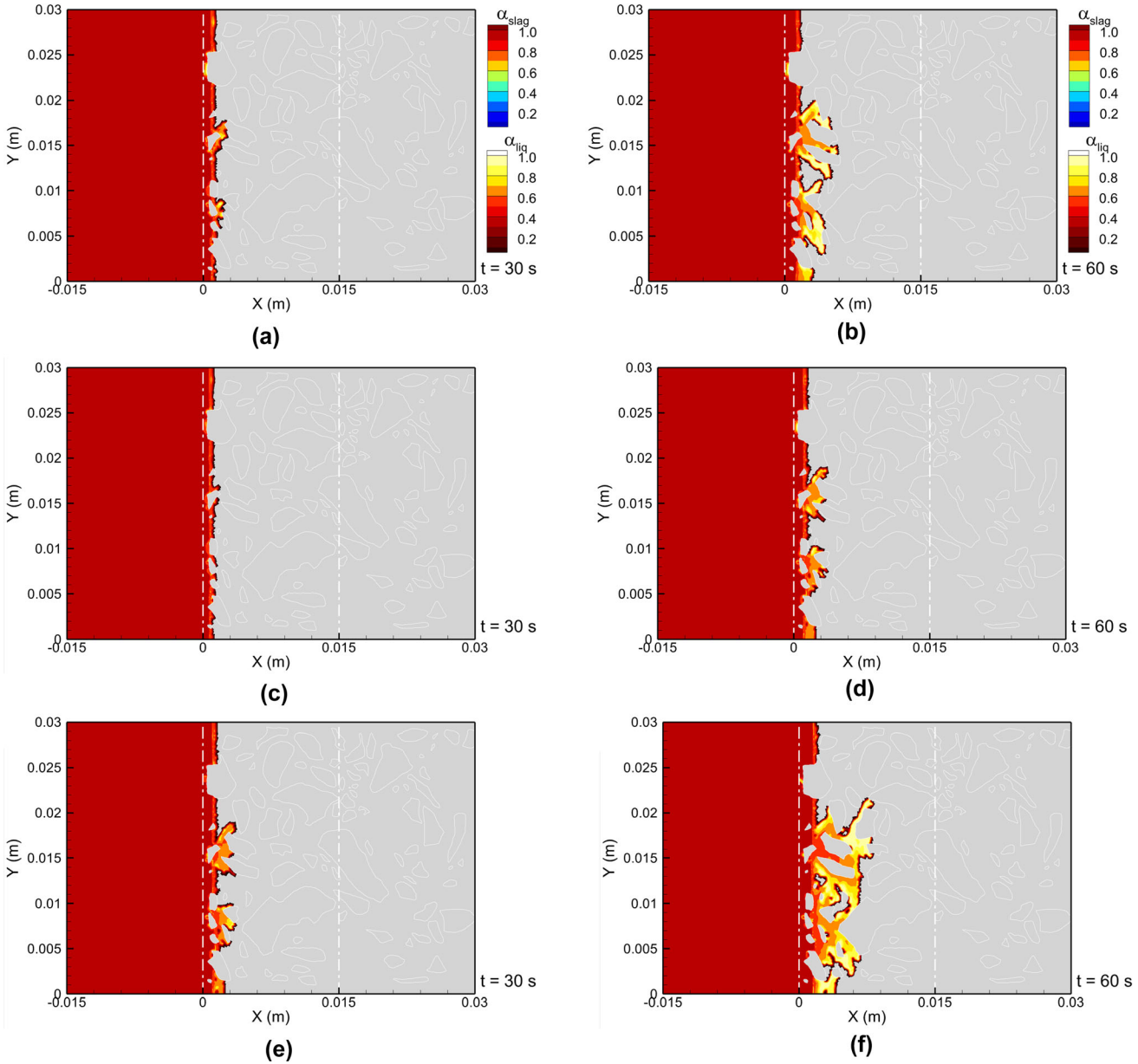

Fig. 11—Corrosion and penetration layer of slag into refractory with different refractory properties: (a), (b) $\varepsilon = 0.14$, $r_m = 6$ μm; (c), (d) $\varepsilon = 0.28$, $r_m = 3$ μm; (e), (f) $\varepsilon = 0.28$, $r_m = 6$ μm.
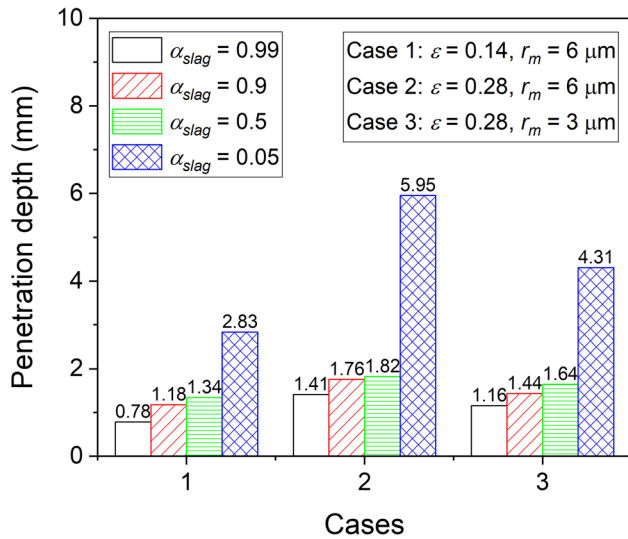
Fig. 12—Penetration depth of slag into refractory with different refractory properties at 60 s.

most severe corrosion occurs when the porosity is 0.28, and the mean pore radius is 6 μm, as depicted in Figures 11(e) and (f).

Furthermore, the summary of corrosion and penetration depth of molten slag into the refractory under varied refractory properties is compared in Figure 12. The penetration distance at 60 seconds, calculated for four different slag volume fractions, is plotted. For corrosion damage (α_{slag} = 0.99), reducing the porosity from 0.28 to 0.14 weakens corrosion from 1.41 to 0.78 mm, a reduction of 44.7 pct. Similarly, decreasing the pore radius from 6 to 3 μm reduces corrosion depth from 1.41 to 1.16 mm, a decrease of 17.7 pct. Additionally, the penetration distance (α_{slag} = 0.05) for a porosity of 0.14 is 2.83 mm, reduced from 5.95 mm for a porosity of 0.28, a reduction of 52.4 pct. Similarly, a smaller porous radius is beneficial in reducing infiltration to 4.31 mm, a decrease of 27.6 pct. Reducing porosity is more effective in controlling molten slag penetration.

V. CONCLUSIONS

In this study, a mathematical model of CaO–Al$_2$O$_3$–MeO slag penetration into Al$_2$O$_3$–MgO refractory was established, considering the porous structure of the matrix in the refractory. The capillary force, as well as the viscous and inertial resistance within the porous matrix, co-determined the penetration and corrosion processes. Based on the validated mathematical model, comparisons were made with varying porosities and mean pore radii, leading to the following conclusions:

1. The molten slag initially spreads into the refractory, passing through some aggregate particles and continuing to penetrate into the refractory interior. Small aggregate particles had a minimal impact on slag penetration, causing them to be completely envel-

oped by molten slag and eventually peel off from the refractory.
2. The slag penetration is accompanied by the diffusion of slag components, leading to compound phase transformations following the principle Al$_2$O$_3$ $\rightarrow$ CA$_6$ $\rightarrow$ CA$_2$ $\rightarrow$ (CA) $\rightarrow$ Liquidus. The reaction interface primarily consisted of CA$_6$ and CA$_2$, aligning with the calculated results.
3. Defined by distinct volume fractions of molten slag, the penetration depth (α_{slag} = 0.05) is more than three times the corrosion depth (α_{slag} = 0.99). In the region penetrated by molten slag, part of the matrix metamorphosed into the liquidus phase.
4. The penetration depth increased with the mean pore radius and the porosity of the refractory. Reducing porosity proved more effective in controlling molten slag penetration, leading to a 44.7 pct reduction in corrosion depth when porosity declined from 0.28 to 0.14.

CONFLICT OF INTEREST

On behalf of all authors, the corresponding author states that there is no conflict of interest.

REFERENCES

1. P. Lian, A. Huang, H. Gu, Y. Zou, L. Fu, and Y. Wang: *Ceram. Int.*, 2018, vol. 44, pp. 1675–80.
2. A. Pack, S. Hoernes, T. Walther, and R. Bross: *Eur. J. Mineral.*, 2003, vol. 15, pp. 193–205.
3. S. Jansson, V. Brabie, and P. Jönsson: *Scand. J. Metall.*, 2005, vol. 34, pp. 283–92.
4. C. Liu, X. Gao, S. Ueda, M. Guo, and S.-Y. Kitamura: *ISIJ Int.*, 2020, vol. 60, pp. 1835–48.
5. Y.-Z. Huo, H. Gu, J. Yang, A. Huang, and Z. Ma: *J. Iron. Steel Res. Int.*, 2022, vol. 29, pp. 1110–18.
6. K. Sarath Chandra and D. Sarkar: *J. Eur. Ceram. Soc.*, 2021, vol. 41, pp. 3782–97.
7. P. Shen, L. Zhang, and Y. Wang: *Metall. Res. Technol.*, 2016, vol. 113, p. 503.
8. J. Wang, L. Zhang, S. Yang, Y. Chen, J. Li, and A. Wachsman: *J. Manuf. Sci. Prod.*, 2013, vol. 13, pp. 133–43.
9. A. Huang, H. Gu, Z. Yang, L. Fu, P. Lian, and L. Jin: *Advanced and Refractory Ceramics for Energy Conservation and Efficiency*, Wiley, Vancouver, 2016, pp. 101–11.
10. L. Fu, H. Gu, A. Huang, S.W. Or, Y. Zou, Y. Zou, and M. Zhang: *J. Eur. Ceram. Soc.*, 2022, vol. 42, pp. 744–63.

11. L. Fu, H. Gu, A. Huang, and H. Ni: *Ceram. Int.*, 2018, vol. 44, pp. 14076–81.
12. L. Fu, H. Gu, A. Huang, M. Zhang, Z. Li, and B. Lee: *J. Am. Ceram. Soc.*, 2015, vol. 98, pp. 1658–63.
13. Z. Liu, J. Yu, S. Yue, D. Jia, E. Jin, B. Ma, and L. Yuan: *Ceram. Int.*, 2020, vol. 46, pp. 3091–98.
14. X. Jia, L. Tian, S. Mao, X. Zhou, S. Chen, and G. Li: *Ceram. Int.*, 2021, vol. 47, pp. 31407–12.
15. K. Mukai: *ISIJ Int.*, 1992, vol. 32, pp. 19–25.
16. L. Cheng, L. Zhang, and P. Shen: *Chin. J. Eng.*, 2018, vol. 40, pp. 1139–57 (**In Chinese**).
17. J. Guarco, S. Vollmann, H. Harmuth, and Burhanuddin: *Mater. Today Commun.*, 2022, vol. 33, p. 104736.
18. Y. Liang, A. Huang, X. Zhu, H. Gu, and L. Fu: *Ceram. Int.*, 2015, vol. 41, pp. 8149–54.
19. T. Matsushita, T. Ohuchi, K. Mukai, I. Sasaka, and J. Yoshitomi: *Taikabutsu Overseas*, 2003, vol. 23, pp. 15–19.
20. K. Mukai, Z. Tao, K. Goto, Z. Li, and T. Takashima: *Scand. J. Metall.*, 2002, vol. 31, pp. 68–78.
21. J. Berjonneau, P. Prigent, and J. Poirier: *Ceram. Int.*, 2009, vol. 35, pp. 623–35.
22. Z. Yang, G. Huazhi, H. Ao, and Z. Meijie: *China's Refract.*, 2017, vol. 26, pp. 17–23.
23. E.Y. Sako, M.A.L. Braulio, E. Zinngrebe, S.R. van der Laan, and V.C. Pandolfelli: *J. Am. Ceram. Soc.*, 2012, vol. 95, pp. 1732–40.
24. A.G. Tomba Martinez, A.P. Luz, M.A.L. Braulio, and V.C. Pandolfelli: *Ceram. Int.*, 2015, vol. 41, pp. 4714–25.
25. M.A.L. Braulio, A.G.T. Martinez, A.P. Luz, C. Liebske, and V.C. Pandolfelli: *Ceram. Int.*, 2011, vol. 37, pp. 1935–45.
26. H. Harmuth and G. Xia: *Trans. Iron Steel Inst. Jpn.*, 2015, vol. 55, pp. 775–80.
27. H. Run, Q. Xing, L. Xiaodong, L. Pengsheng, and Z. Jinzhu: *Refract. Ind. Ceram.*, 2018, vol. 59, pp. 134–39.
28. M.H. Moreira, S.D. Pont, R.F. Ausas, A.P. Luz, T.M. Cunha, C. Parr, and V.C. Pandolfelli: *Ceram. Int.*, 2021, vol. 47, pp. 28086–28105.
29. Q. Wang, C. Tan, A. Huang, W. Yan, H. Gu, Z. He, and G. Li: *Metall. Mater. Trans. B*, 2021, vol. 52B, pp. 1344–56.
30. Q. Wang, C. Liu, L. Pan, Z. He, G. Li, and Q. Wang: *Metall. Mater. Trans. B*, 2022, vol. 53B, pp. 1617–30.
31. A.O. Huang, H. Gu, M. Zhang, N. Wang, T. Wang, and Y. Zou: *Metall. Mater. Trans. B*, 2013, vol. 44B, pp. 744–49.
32. I. Özdemir, W.A.M. Brekelmans, and M.G.D. Geers: *J. Eur. Ceram. Soc.*, 2010, vol. 30, pp. 1585–97.
33. S. Samadi, S. Jin, D. Gruber, and H. Harmuth: *Finite Elem. Anal. Des.*, 2022, vol. 206, p. 103762.
34. Q. Wang, S. Jia, G. Li, Y. Li, T. Wang, and Z. He: *ISIJ Int.*, 2020, vol. 60, pp. 1938–47.
35. K. Feng, A. Liu, K. Dai, S. Feng, J. Ma, J. Xie, B. Wang, Y. Yu, and J. Zhang: *Powder Technol.*, 2017, vol. 314, pp. 649–59.
36. S. Ergun: *Ind. Eng. Chem. Res.*, 1952, vol. 20, pp. 1196–1200.
37. *Ansys Fluent Users Guide*. ANSYS, Inc., 2022.
38. Y. Zou: Wuhan University of Science and Technology, 2014 (**In Chinese**).
39. J.Y. Choi and H.G. Lee: *Trans. Iron Steel Inst. Jpn.*, 2003, vol. 43, pp. 1348–55.
40. C.W. Bale, E. Bélisle, P. Chartrand, S.A. Decterov, G. Eriksson, A.E. Gheribi, K. Hack, I.H. Jung, Y.B. Kang, J. Melançon, A.D. Pelton, S. Petersen, C. Robelin, J. Sangster, P. Spencer, and M.A. Van Ende: *Calphad*, 2016, vol. 54, pp. 35–53

.